Supplement of Biogeosciences, 20, 3981–3995, 2023
https://doi.org/10.5194/bg-20-3981-2023-supplement

Biogeosciences Open Access EGU

Supplement of

The response of wildfire regimes to Last Glacial Maximum carbon dioxide and climate

Olivia Haas et al.

Correspondence to: Olivia Haas (o.haas20@imperial.ac.uk)

S1. Obtaining Fraction of Absorbed Photosynthetically Active Radiation (fAPAR) from BIOME4.

BIOME4 (Kaplan et al., 2003) is a coupled biogeography and biogeochemistry with which we can simulate the equilibrium distribution of biomes from latitude, atmospheric CO_2 concentration, mean monthly precipitation, temperature, and cloud cover. On of the outputs provided by the model is monthly leaf area index (LAI), which we can convert to Fraction of Absorbed Photosynthetically Active Radiation (fAPAR) using Beer-Lamberth law:

$$\text{fAPAR} = 1 - \exp(-k.\ \text{LAI}) \quad (2)$$

where k ≈ 0..5, a constant extinction coefficient (Saitoh et al., 2012).

fAPAR simulated from BIOME4 under modern-day conditions (2010-2015 seasonal climatology; Cucchi et al., 2020) overestimated fAPAR compared to observed fAPAR from NASA/GIMMS fAPAR 3g from the same period. As such, we rescaled the simulated BIOME fAPAR for each experiment such that:

$$fAPAR_{rescaled} = fAPAR_{exp} \frac{fAPAR_{obs}}{fAPAR_{sim}}) \quad (3),$$

$where\ fAPAR_{rescaled}$ is the monthly rescaled fAPAR for that experiment, $fAPAR_{exp}$ is the original fAPAR output from BIOME4 for that experiment and $\frac{fAPAR_{obs}}{fAPAR_{sim}}$ is a constant scaling factor, determined for each biome, where $fAPAR_{obs}$ is the monthly NASA/GIMMS fAPAR 3g median value for that biome, and $fAPAR_{sim}$ is the monthly fAPAR median value simulated by BIOME4 for that biome. This method provided a rescaled fAPAR for the modern day that was correlated at 0.63 with the observational data, compared to 0.13 for the original BIOME4 fAPAR output for the same period, a reasonable estimation of fAPAR for each of the experiments.

S2. Human sensitivity experiments for modern and LGM conditions

Since we were interested in isolating out the effect of different climate and CO_2 scenarios in driving global pattern of burnt area (BA), fire size (FS) and fire intensity (FI), it was essential to ensure no confounding effects were introduced through the presence of predictors related to human activity.

Setting human predictors to zero under modern conditions had no effect on FI but a strong effect on BA and FS, leading to large increases when human activity was "off" (see Table S.2.1). However, increase in BA and FS at the modern was driven by road density and to a lesser extent cropland, not human population. This was expected as the original GLM models are not very sensitive to human population alone (Haas et al., 2022). The limited impact of population density in driving global fire regimes in the GLM models is in line with research showing the importance of anthropogenic landscape fragmentation when modelling how humans influence fire regimes, as opposed to focusing solely on the effect of human population (e.g. Bistinas et al., 2014, Knorr et al 2014, 2016; Kelley et al., 2019; Harrison et al., 2021).

Table S.2.1. Sensitivity of GLM models to human activity using both observations and BIOME4 derived vegetation and GPP.

Although there are global reconstructions of human population density for the Holocene (e.g. HYDE, KK10), these are poorly constrained before the past 2-3 thousand years, as is shown by the marked differences between existing global maps. Uncertainty is even greater regarding population densities at the LGM. As such, we did not deem it feasible to run a global sensitivity analysis to assess the sensitivity of LGM fire regimes to human activity. However, we did run three regional analysis (Europe, Africa and Australia) at the LGM with human population (LGM climate/LGM CO_2 popd) and without (LGM climate/LGM CO_2) and compared the amplitude of change between these two experiments with the amplitude of change between the realistic LGM experiment (LGM climate/LGM CO_2) and the realistic modern experiment (MOD climate/MOD CO_2). This allowed us to assess whether setting human population densities to zero had a significant impact on the LGM and whether it had the potential to influence the global trends between the LGM and the MOD experiments. For the European experiment, we used the gridded data produced by Tallavaara et al., (2015). For the African and Australian experiments, we used the estimated population densities from Gautney and Holliday (2015) for areas that were considered habitable and set the population density to zero in areas considered uninhabitable. We considered an area uninhabitable when it was a modelled as desert or barren by BIOME4 (Kaplan et al., 2003) or was at an altitude above 3000 m, following the methodology by Gautney and Holliday (2015). We compared our total and habitable areas to the estimates of Gautney and Holliday (2015). Although there were some differences, they were reasonably similar (see Table 1; Figure 1).

Inputs for land cover and P Model GPP (Cucchi et al., 2020)	**ESA CCI Landcover NASA/GIMS fAPAR 3g**	**BIOME4 (Kaplan et al., 2003)**	**Global estimates from the literature**
Burnt area (millions km²)			
Human activity on	4.42	4.25	[1.87 – 4.6] (Humber et al., 2019)
Human activity off	7.41	11.27	
% change	40.35	62.29	
Fire size (km²)			
Human activity on	3.36	3.61	4.4 (Andela et al., 2019) (does not include wildfires smaller than 0.21 km²)
Human activity off	5.34	6.25	
% change	37.08	42.24	
Fire intensity (W.km^{-1})			
Human activity on	40.00	31.41	
Human activity off	39.20	31.17	
% change	− 2.04	− 0.77	

Table S.2.2. Habitable land area and population estimates for Africa and Australia

	Africa				Australia			
	Total land area (km^2)	Habitable (km^2)	% Habitable	Number of people	Total land area (km^2)	Habitable (km^2)	% Habitable	Number of people
AWIESM1	34,028,261	20,982,697	62%	2,566,184	9,456,315	6,051,339	64%	30,257
MPI-ESM1.2	34,071,392	21,553,863	63%	2,636,037	9,456,315	7,048,721	75%	32,995
CESM1.2	34,322,097	22,199,317	65%	2,714,976	9,421,515	6,599,033	70%	32,995
Gautney and Holliday (2015)	30,493,900	12,846,597	42%	1,571,139	11,021,024	9,418,730	85%	47,093

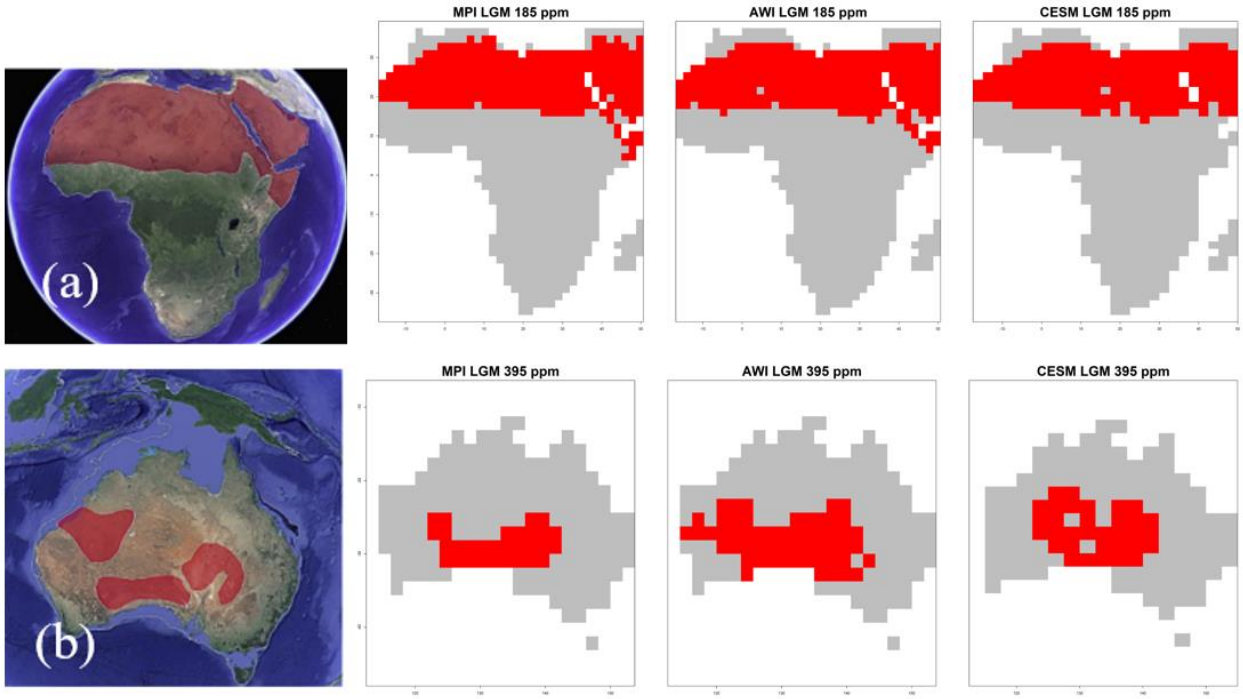

Figure S.2.1. Maps of deserted areas at the LGM (shown in red) (a) showing the extent of the Sahara and Arabian Deserts according to Gautney and Holliday (2015), (b) showing the Great Victorian Desert, the Simpson Desert, and the Great and Little Sandy Deserts according to Gautney and Holliday (2015), (c) showing the extent of desert and barren simulated by BIOME4 for Africa and (d) showing the extent of desert and barren areas simulated by BIOME4 for Australia

Although some hunter-gatherer communities foraged for plants at the LGM (Liu et al., 2013), there is large uncertainty surrounding the extent of this practice at a global scale. Additionally, cropland in the GLMs is understood as a large-scale landscape feature, significant at least a ~ 55km resolution at the equator. It is reasonable to assume that hunter-gatherer communities at the LGM did not cultivate crops on this scale. Roads and crop cover were therefore set to zero under all LGM experiments, including the experiment with human population estimates.

We observed very slight differences between the regional LGM experiments when human population densities were included and when they were not (less than 5% change for BA, FS and FI). These differences were much smaller than the differences between the LGM experiment and the MOD experiment (see Table 2).

Table S2.3. Regional BA, FS and FI estimates for MOD climate/MOD CO_2, LGM climate/LGM CO_2 and LGM climate/LGM CO_2 popd

	AWI-ESM1			**MPI-ESM1.2**			**CESM1.2**		
	Europe	Africa	Australia	Europe	Africa	Australia	Europe	Africa	Australia
Burnt area (km^2)									
MOD climate/MOD CO_2,	101,041	6,568,740	1,491,914	99,222	6,439,953	1,441,669	97,967	6,323,321	1,490,743
LGM climate/LGM CO_2	20,124	3,099,159	2,108,874	22,494	1,410,410	1,135,466	10,409	1,534,357	886,142
LGM climate/LGM CO_2 popd	20,210	3,114,700	2,113,961	22,603	1,417,576	1,138,501	10,500	1,542,090	890,406
% change between MOD and LGM	− 80	− 53	41	− 77	− 78	− 21	− 89	− 76	− 41
% change between LGM and LGM popd	0.43	0.50	0.24	0.48	0.27	− 0.85	− 0.85	0.50	0.48
Fire size (km^2)									
MOD climate/MOD CO_2,	5.12	8.88	11.07	4.97	9.33	11.96	6.07	9.22	12.79
LGM climate/LGM CO_2	6.51	9.05	12.93	5.97	7.98	11.87	7.32	7.52	13.72
LGM climate/LGM CO_2 popd	5.51	9.05	12.93	5.97	7.98	11.87	7.51	7.52	13.72
% change between MOD and LGM	27	2	17	20	14	0.75	21	− 18	7
% change between LGM and LGM popd	0	0	0	0	0	0	0	0	0
Fire intensity ($W.km^{-1}$)									

MOD climate/MOD CO_2,	29.97	16.65	20.80	30.43	16.48	20.09	27.19	16.74	19.63
LGM climate/LGM CO_2	37.66	17.90	18.14	37.16	20.56	21.81	41.39	23.68	29.89
LGM climate/LGM CO_2 popd	37.62	17.81	18.05	37.13	20.46	21.71	44.61	23.53	29.75
% change between MOD and LGM	26	8	− 9	22	25	9	52	41	52
% change between LGM and LGM popd	− 0.1	− 0.5	− 4.5	− 0.1	− 0.5	− 0.5	− 0.5	− 0.6	− 0.5

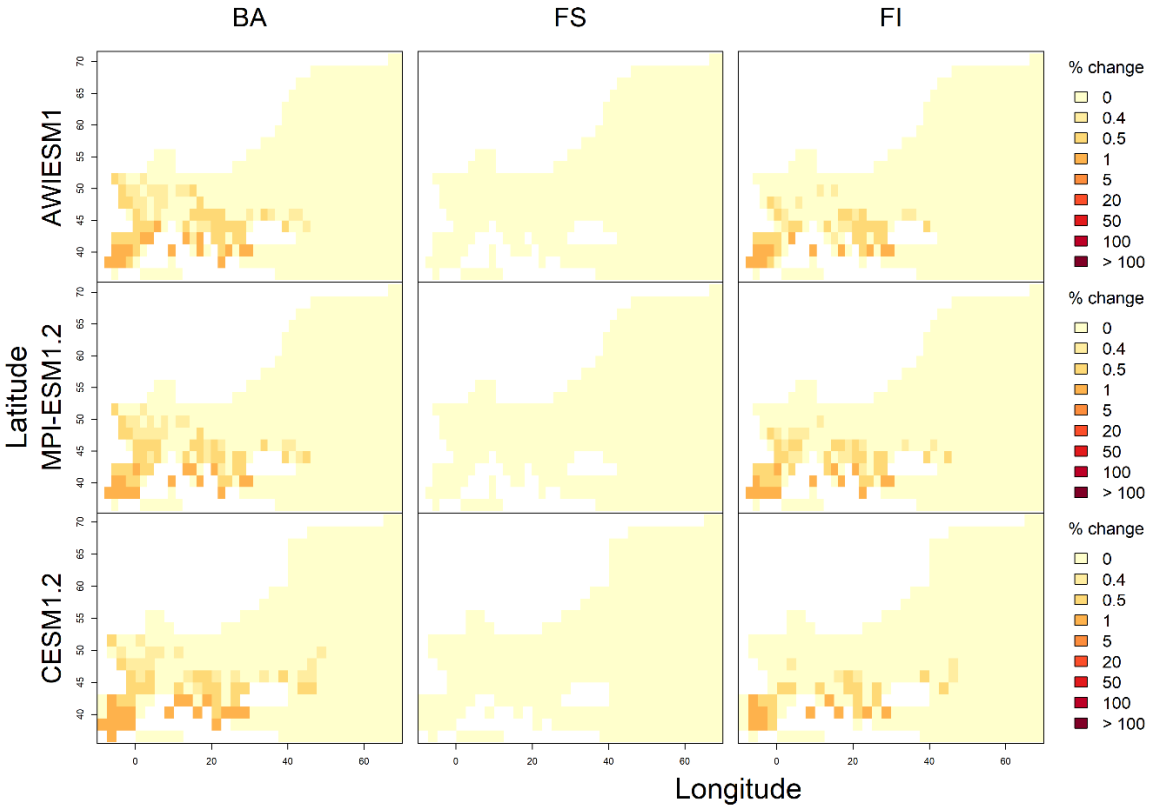

Figure S.2.2. Percentage change of BA, FS and FI when including population estimates at the LGM for Europe

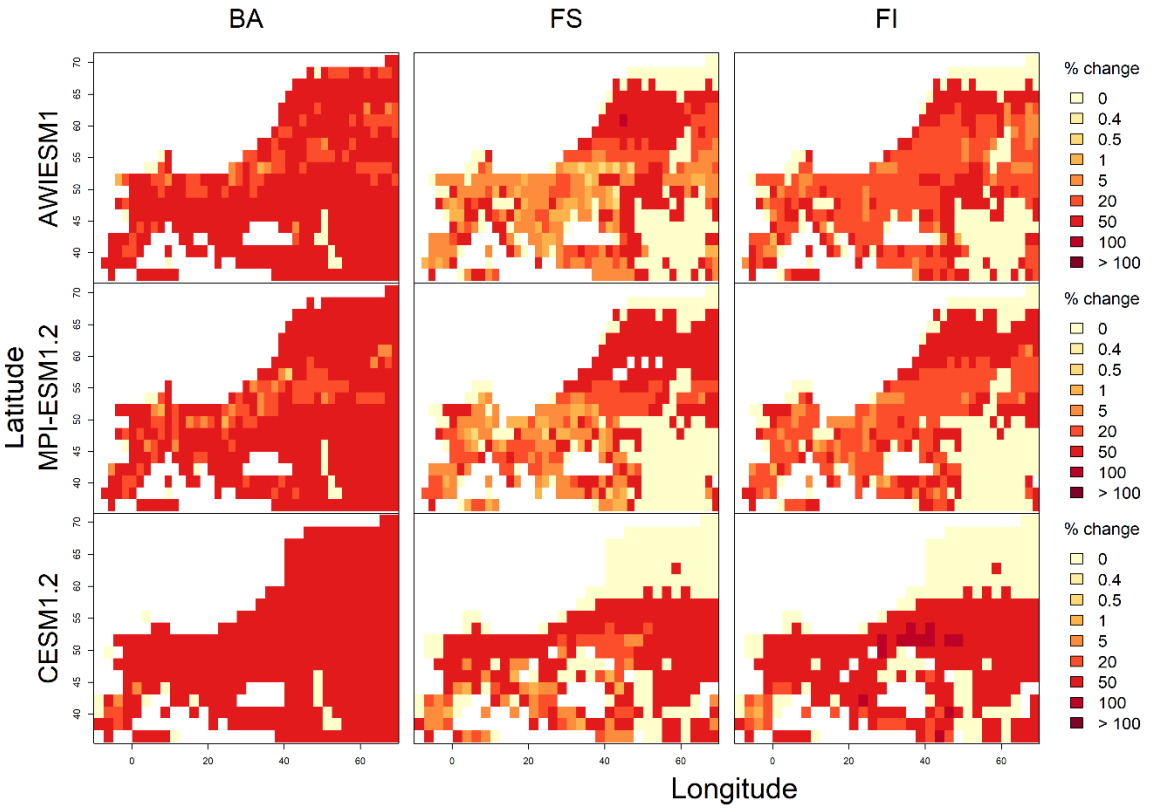

Figure S.2.3. Percentage change of BA, FS and FI between the realistic LGM experiment (LGM climate/LGM CO_2) and the realistic modern experiment (MOD climate/MOD CO_2) for Europe

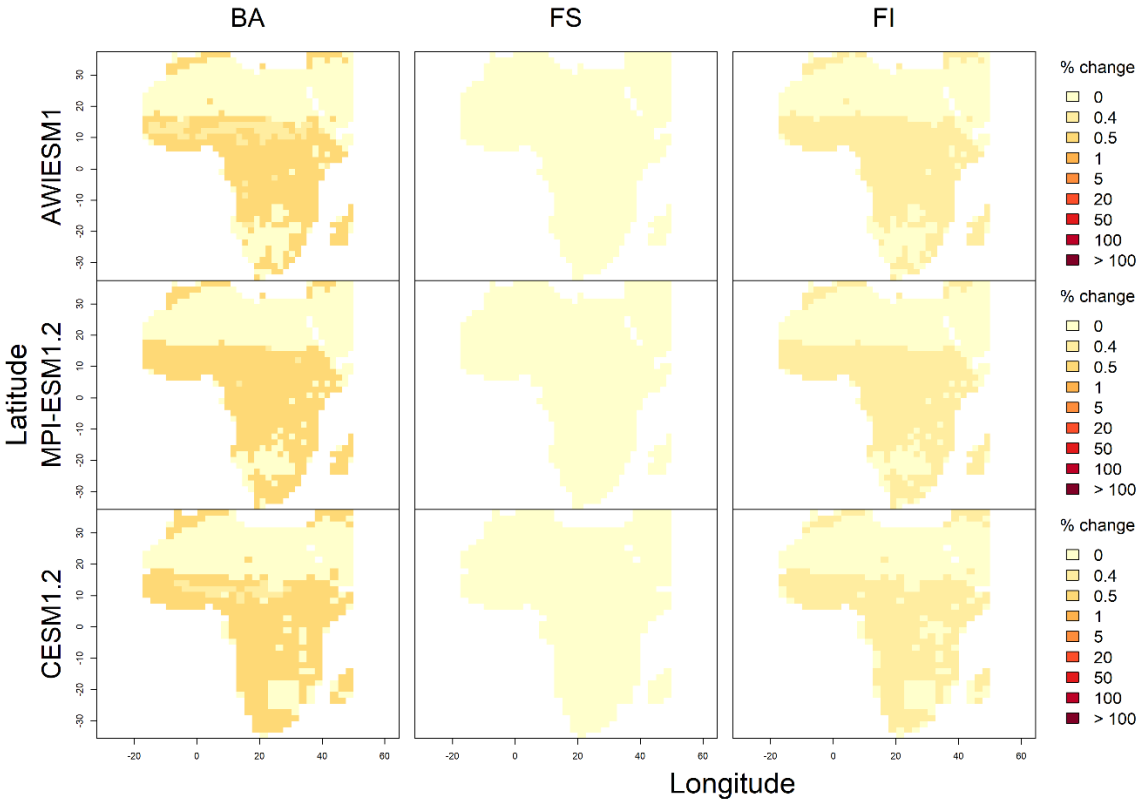

Figure S.2.4. Percentage change of BA, FS and FI when including population estimates at the LGM for Africa

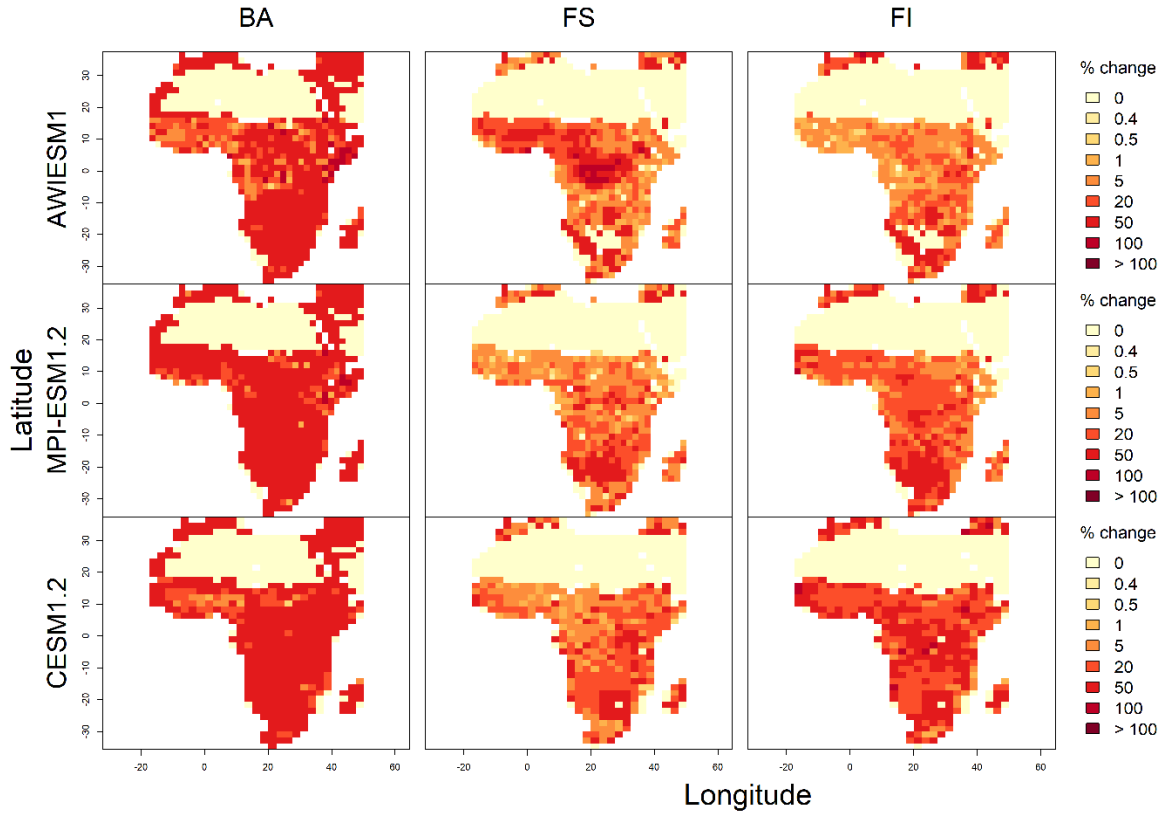

Figure S.2.5. Percentage change of BA, FS and FI between the realistic LGM experiment (LGM climate/LGM CO_2) and the realistic modern experiment (MOD climate/MOD CO_2) for Africa

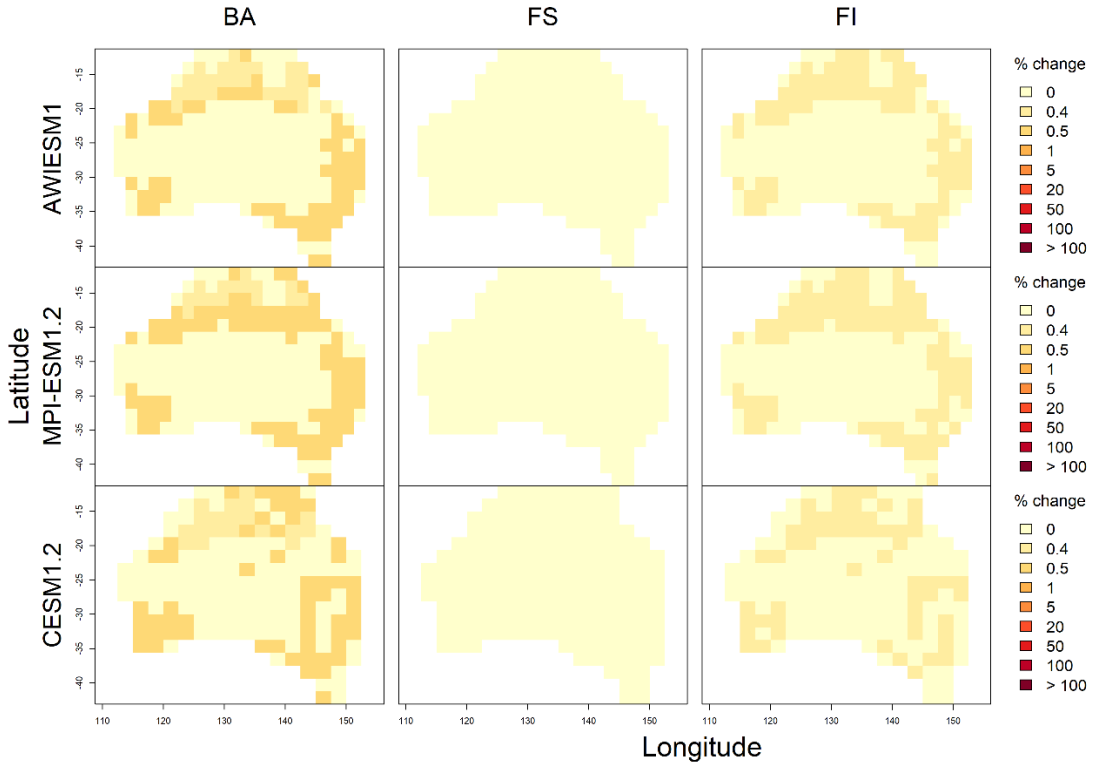

Figure S.2.6. Percentage change of BA, FS and FI when including population estimates at the LGM for Australia

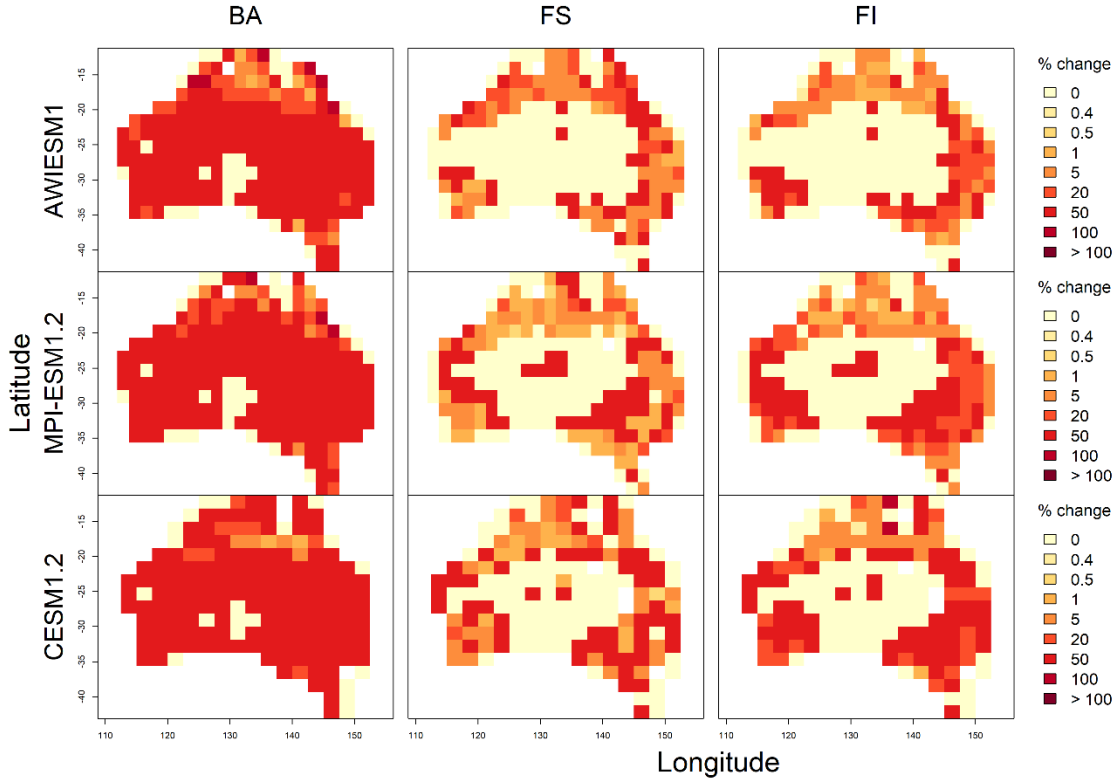

Figure S.2.7. Percentage change of BA, FS and FI between the realistic LGM experiment (LGM climate/LGM CO_2) and the realistic modern experiment (MOD climate/MOD CO_2) for Australia

The results of these sensitivity analysis, combined with the large uncertainty associated with human population numbers at the LGM, justify our approach of setting human predictors to zero. In doing so, we are not stating that the effect of human impact was negligible; rather that due to large uncertainties around human activity at the LGM, the most transparent approach is to run all the experiments in a counterfactual "human-less" world, both in the modern and the LGM to focus on the effects of climate and CO_2. The aim of this approach was to eliminate any confounding effect associated with human activity to concentrate on the effects of LGM climate and CO_2 on global fire regimes. Under modern conditions, human activity has been shown to have a negative effect on biomass burning (e.g Pechony and Shindell, 2010; Bowman et al., 2020; Marlon et al., 2008; Wang et al., 2010) with this suppression effect most likely driven by population growth and land-use change leading to increased landscape fragmentation which can suppress fire spread (e.g. Knorr et al., 2014; Andela et al., 2016; Harrison et al., 2021). By setting our human predictors to zero we also account for this suppression effect at the modern. Whilst we could have chosen to include human predictors, since doing so does did not affect overall trends and introduced large uncertainty, we decided against it and believe this approach to be appropriate.

S3. Obtaining burnt area mask for fire size and fire intensity experiments

In this analysis, we were interested in how the global pattern of burnt area (BA), fire size (FS) and fire intensity (FI) change under different climate and CO_2 scenarios. Both the GLM models for FS and FI return values of estimated FS and FI assuming a fire occurs since the models were fitted to observed data for FS and FI. When no fire occurred, there was no data for either FS or FI. As such, these models cannot determine themselves if an ignition occurred.

To study changes in FS and FI, it is necessary to apply an ignition threshold, which we obtained from the BA model. The burnt area (BA) generalized linear model (GLM) provides a robust reconstruction of BA under the model training conditions with a 0.8 correlation between the observational data and the fitted values(Haas et al., 2022). There are no systematic biases evident from plotting the residuals of the model but there is a compression of the range of reconstructed values, leading to apparent over- (under-) prediction at the low (high) extremes. This is to be expected, as the observational values reflect what really happened over the study period. Whilst some exceptionally large/intense wildfires occurred, many grid-cells also had no fire activity whilst the fitted values represent the probability of burning in each grid-cell, regardless of what happened during the study period. We obtained the ignition threshold value by studying the distribution of reconstructed BA values under the original model training period (2010-2015) when the observed BA value is 0, representing 26% of the grid-cells (a total of 14,816 data points and associated fitted values). We then took the median value of these fitted values as a threshold for ignition.

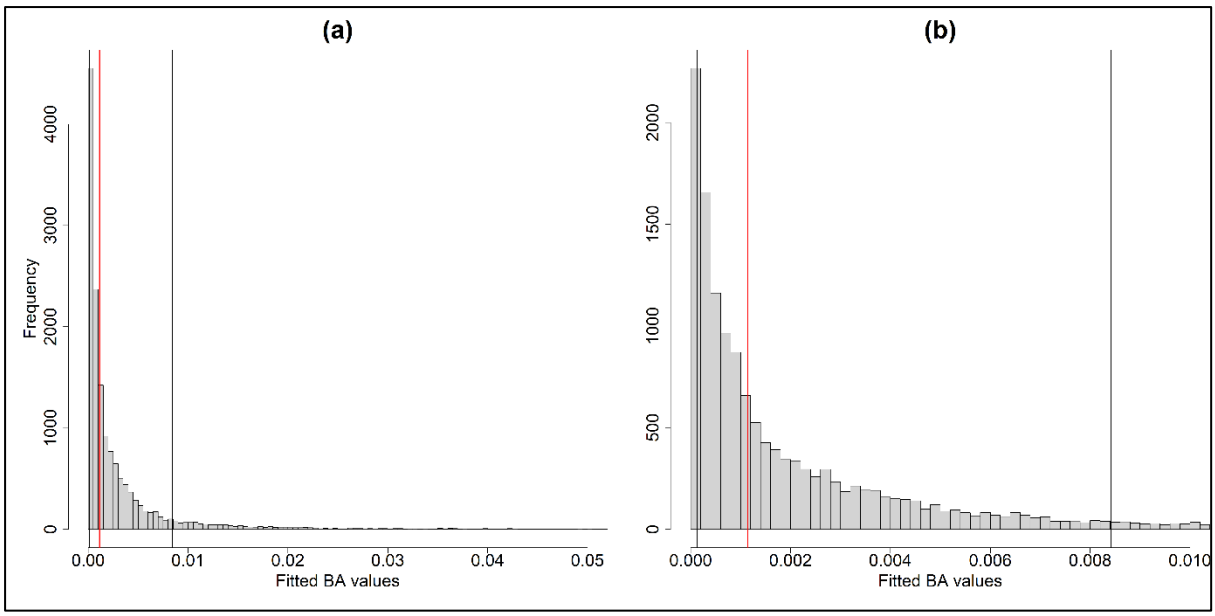

Figure S3.1. Histograms showing the distribution of the fitted values by the GLM BA model when observed BA values are 0 in the 2010-2015 climatology for (a) the whole range and (b) the range up to the 95th percentile. The red line shows the median value, and the black lines show the 10th and 90th percentile values.

	10th percentile	50th percentile	90th percentile
Fitted BA	0.0001	0.0011	0.0084

Table S3.1. Statistics for the fitted BA distribution when observed BA is 0 for the 2010-2015 climatology.

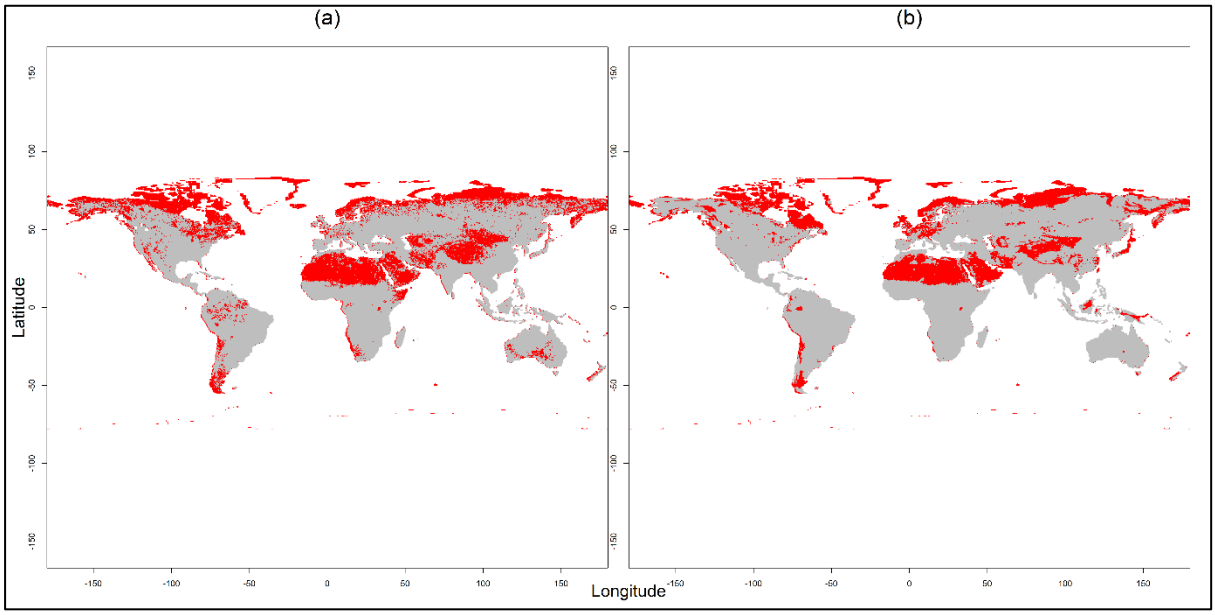

Figure S.3.2. Maps of BA ignition mask (where no burning is assumed to occur) under modern-day conditions (2010-2015 climatology) showing in red (a) where the observational BA values are 0 and (b) where the fitted BA values are equal or lower to 0.0011.

S4. Mapped results from the 12 experiments for all three LGM scenarios.

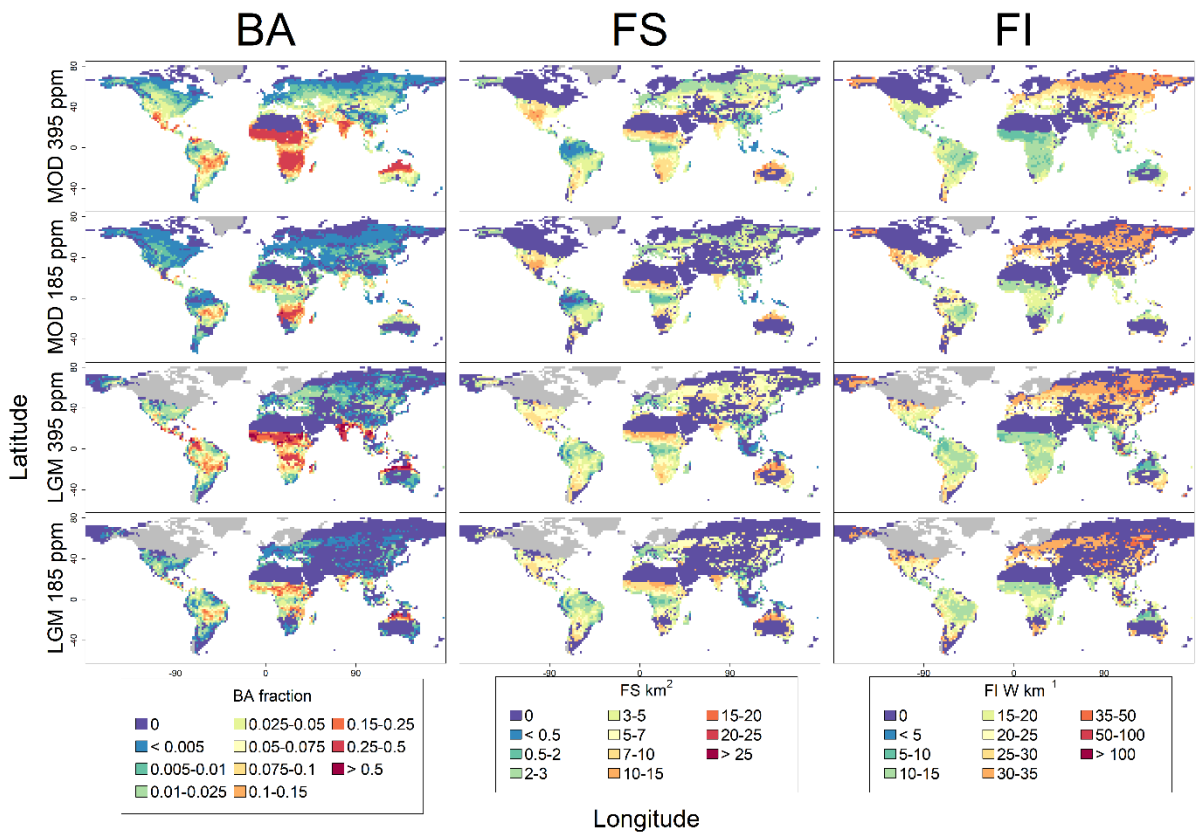

Figure S4.1. Changes in burnt area (BA), fire size (FS) and fire intensity (FI) using modern day climate (MOD) or Last Glacial Maximum (LGM) climate from the MPI-ESM1.2 simulation with either modern (395 ppm) or LGM (185 ppm) CO_2.

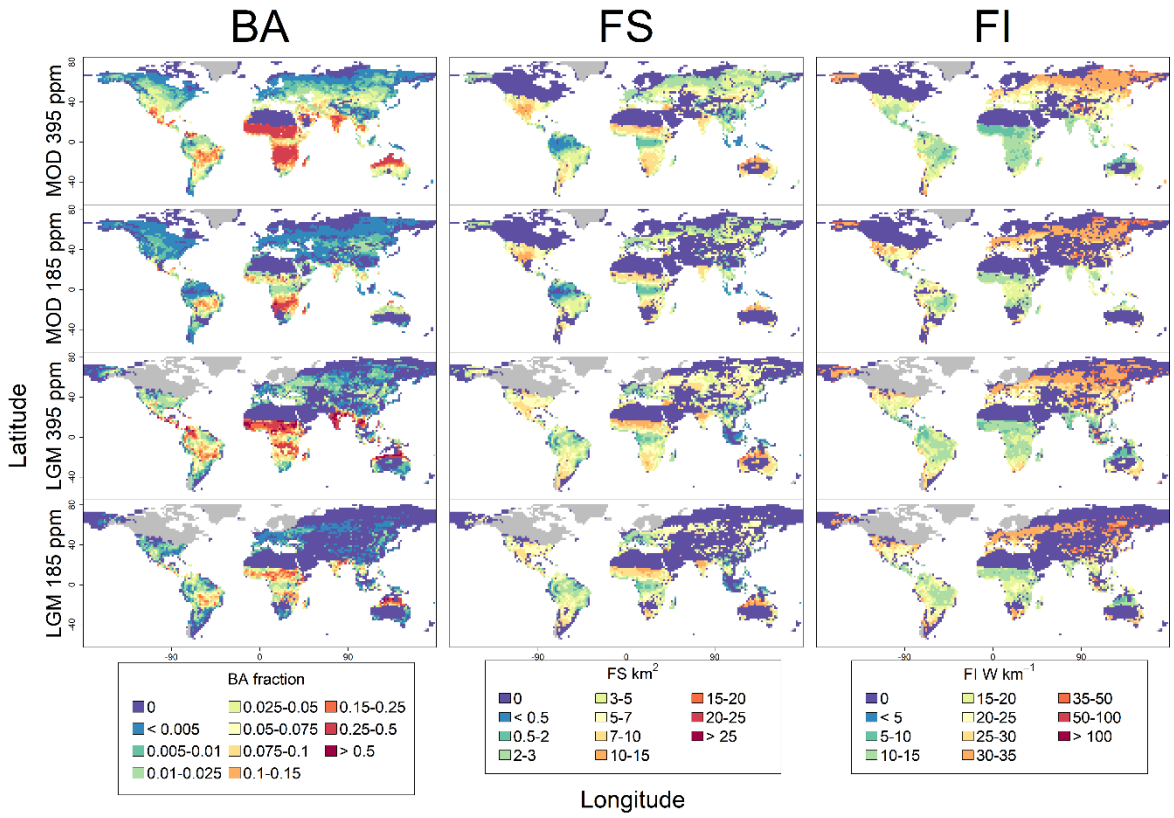

Figure S4.2. Changes in burnt area (BA), fire size (FS) and fire intensity (FI) using modern day climate (MOD) or Last Glacial Maximum (LGM) climate from the AWIESM1 simulation with either modern (395 ppm) or LGM (185 ppm) CO_2.

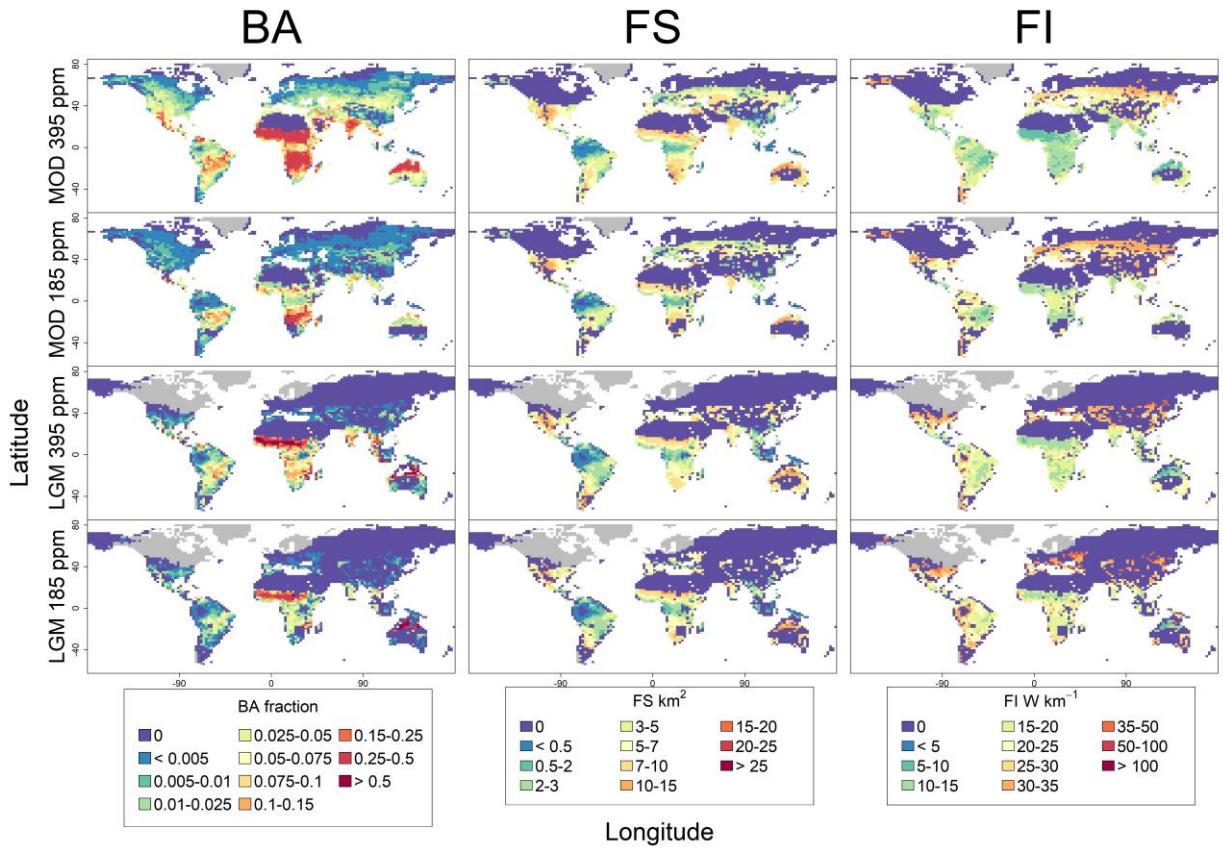

Figure S4.3. Changes in burnt area (BA), fire size (FS) and fire intensity (FI) using modern day climate (MOD) or Last Glacial Maximum (LGM) climate CESM1.2 simulation with either modern (395 ppm) or LGM (185 ppm) CO_2.

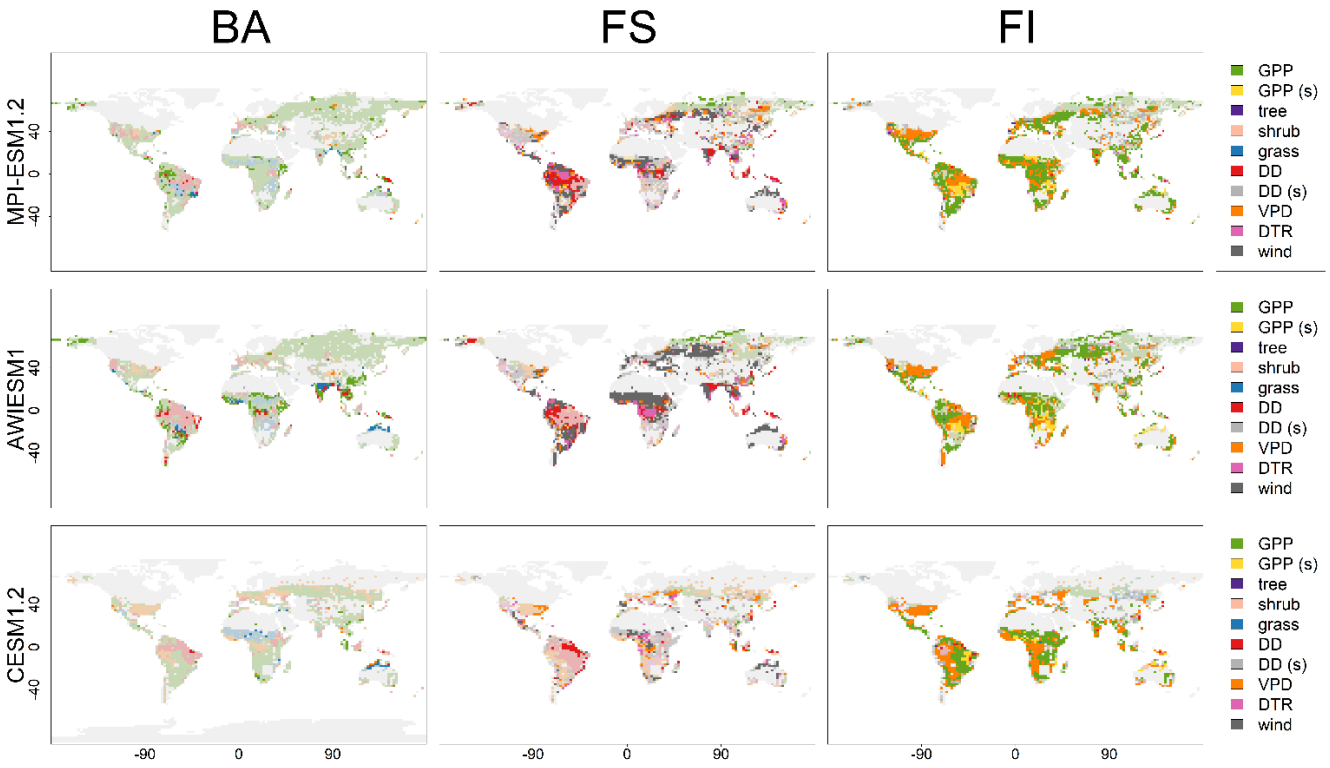

Figure S4.4. Map showing which model variable was responsible for some of the most important grid-cell changes between the realistic modern-day climate (MOD) 395 ppm experiment and the realistic Last Glacial Maximum (LGM) 185 ppm scenarios for BA, FS and FI for (a) the AWIESM1 LGM scenario, (b) the MPI-ESM1.2 LGM scenario and (c) the CESM1.2 LGM scenarios. Faded colors represent that the effect was a negative one, leading to a decrease in the wildfire property at the LGM whilst full colors represent an increase in the wildfire property at the LGM.

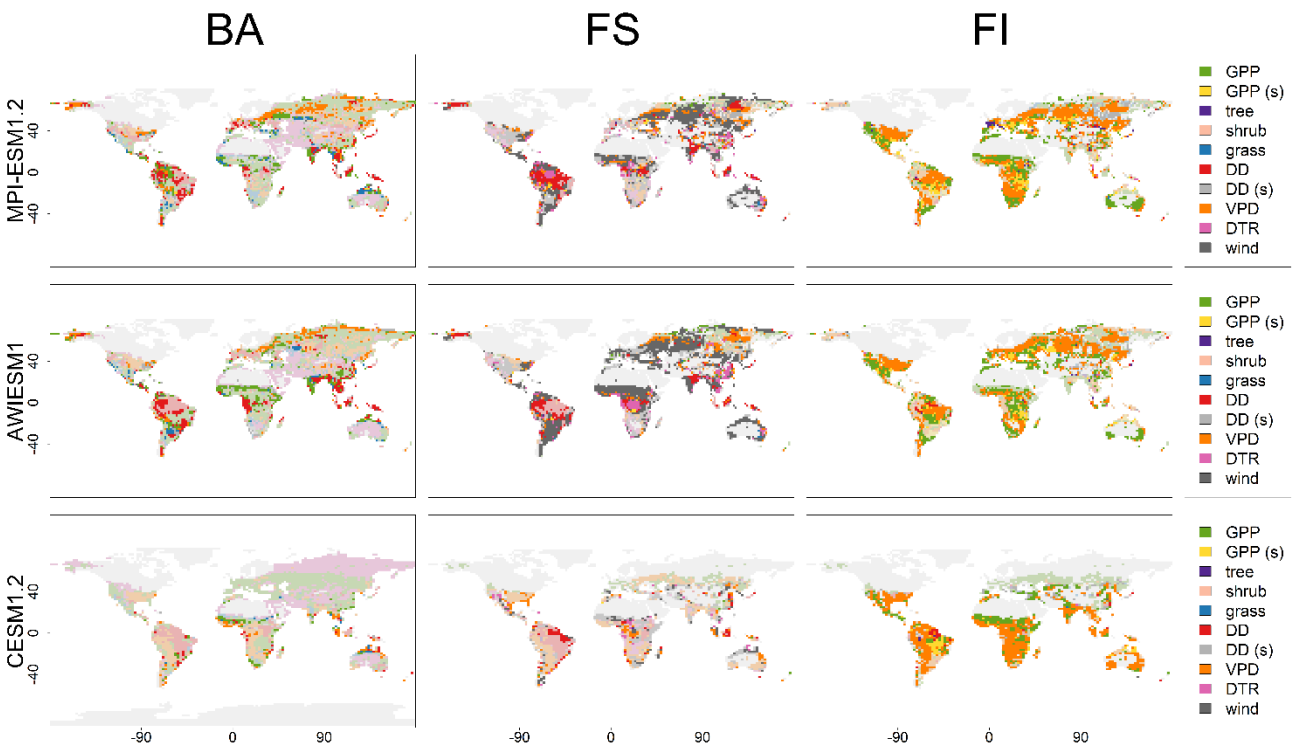

Figure S4.5. Map showing which model variable was responsible for some of the most important grid-cell changes between the MOD 395 ppm and LGM 395 ppm experiment (LGM climate/MOD CO_2) for BA, FS and FI for (a) the AWIESM1 LGM scenario, (b) the MPI-ESM1.2 LGM scenario and (c) the CESM1.2 LGM scenarios. Faded colors represent that the effect was a negative one, leading to a decrease in the wildfire property at the LGM whilst full colors represent an increase in the wildfire property at the LGM.

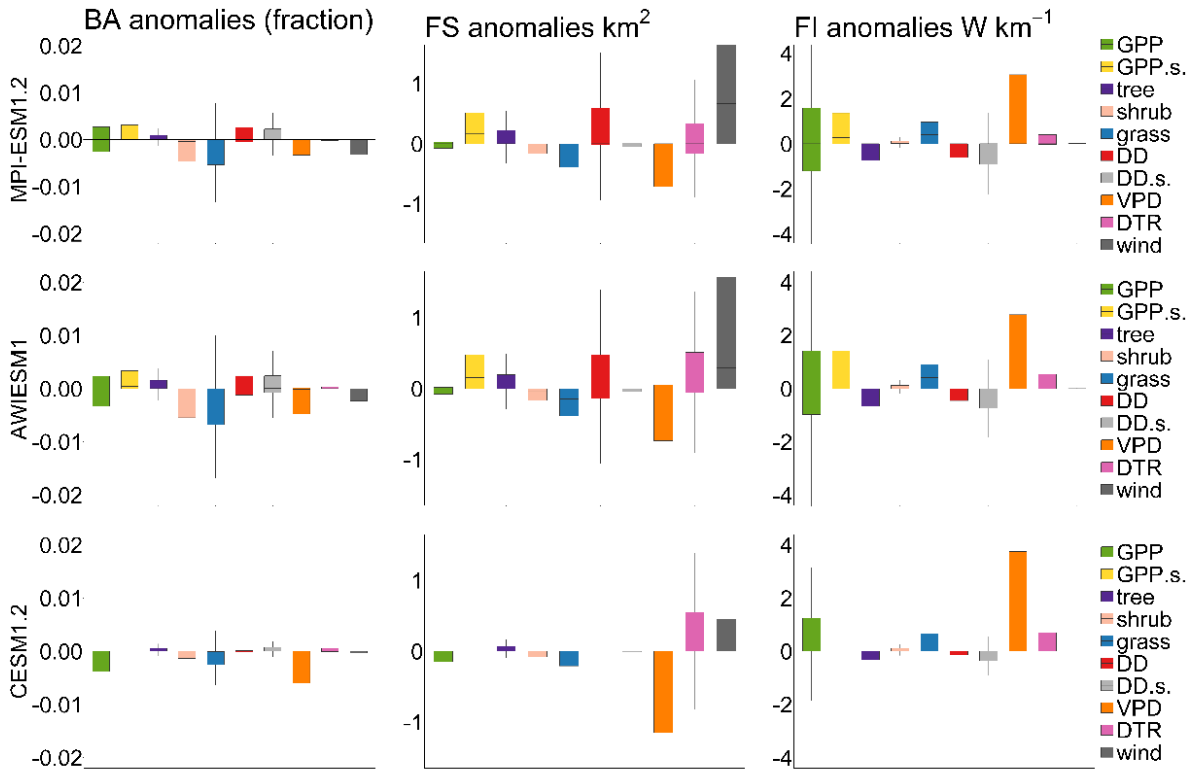

Figure S4.6. Boxplots showing relative importance of each predictor (GPP; gross primary production, GPP.s.; GPP seasonality, tree; tree cover, shrub; shrub cover, grass; grass cover, DD; dry days, DD.s.; dry days seasonality, VPD; vapour pressure deficit, DTR; diurnal temperature range, wind; wind speed) in driving the anomaly between the MOD 395 ppm and LGM 395 ppm experiment. For each grid cell common to both experiments (on modern-day continental shelves and masking the LGM ice sheets), the predictor which cause the largest change in the anomaly between the two experiments when it was excluded from the GLM model was retained, it is the change in anomaly that is shown here. This was taken as an indicator of relative importance of that predictor in driving the observed change for (a) the AWIESM1 LGM scenario, (b) the MPI-ESM-1.2 LGM scenario and (c) the CESM1.2 LGM scenario. A positive anomaly represents the variable driving an increase in BA, FS or FI at the LGM and a negative anomaly represents the variable driving a decrease in BA, FS or FI at the LGM.

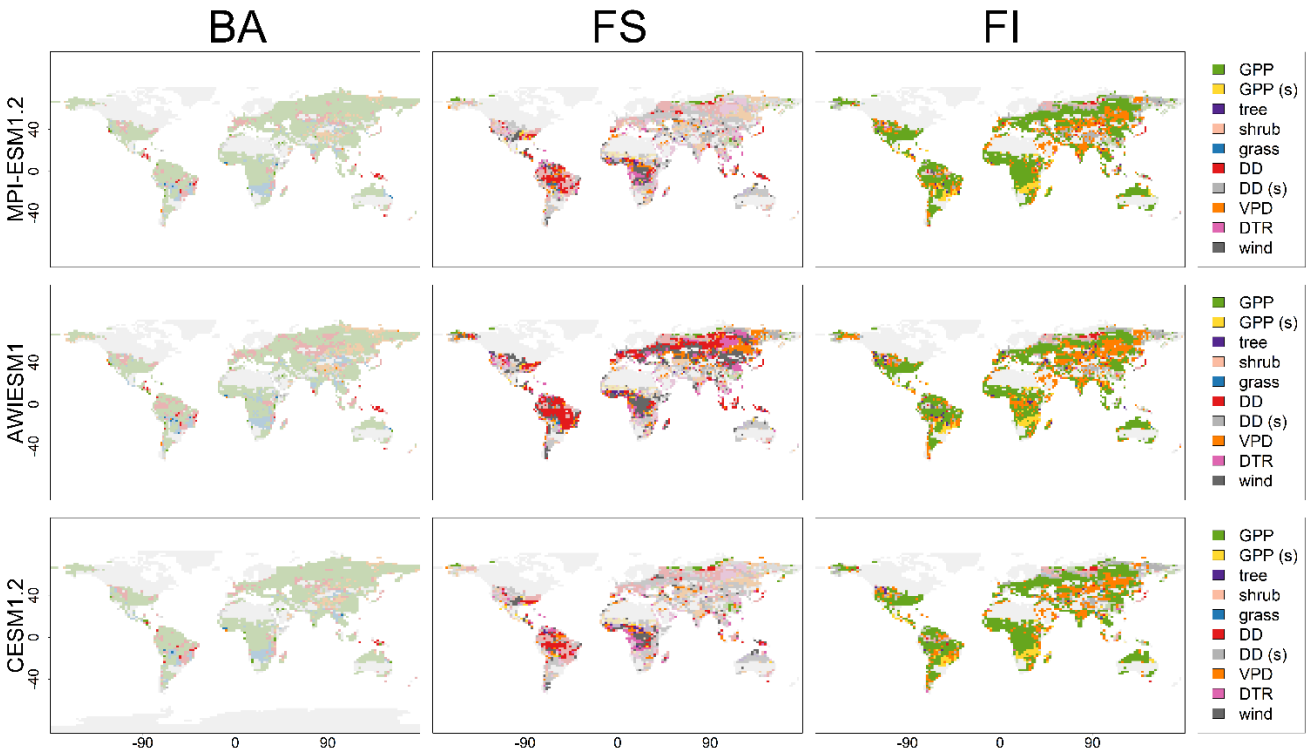

Figure S4.7. Map showing which model variable was responsible for some of the most important grid-cell changes between the realistic MOD 395 ppm and MOD 185 ppm experiment (MOD climate/LGM CO_2) for BA, FS and FI for (a) the AWIESM1 LGM scenario, (b) the MPI-ESM1.2 LGM scenario and (c) the CESM1.2 LGM scenarios. Faded colors represent that the effect was a negative one, leading to a decrease in the wildfire property at the LGM whilst full colors represent an increase in the wildfire property at the LGM.

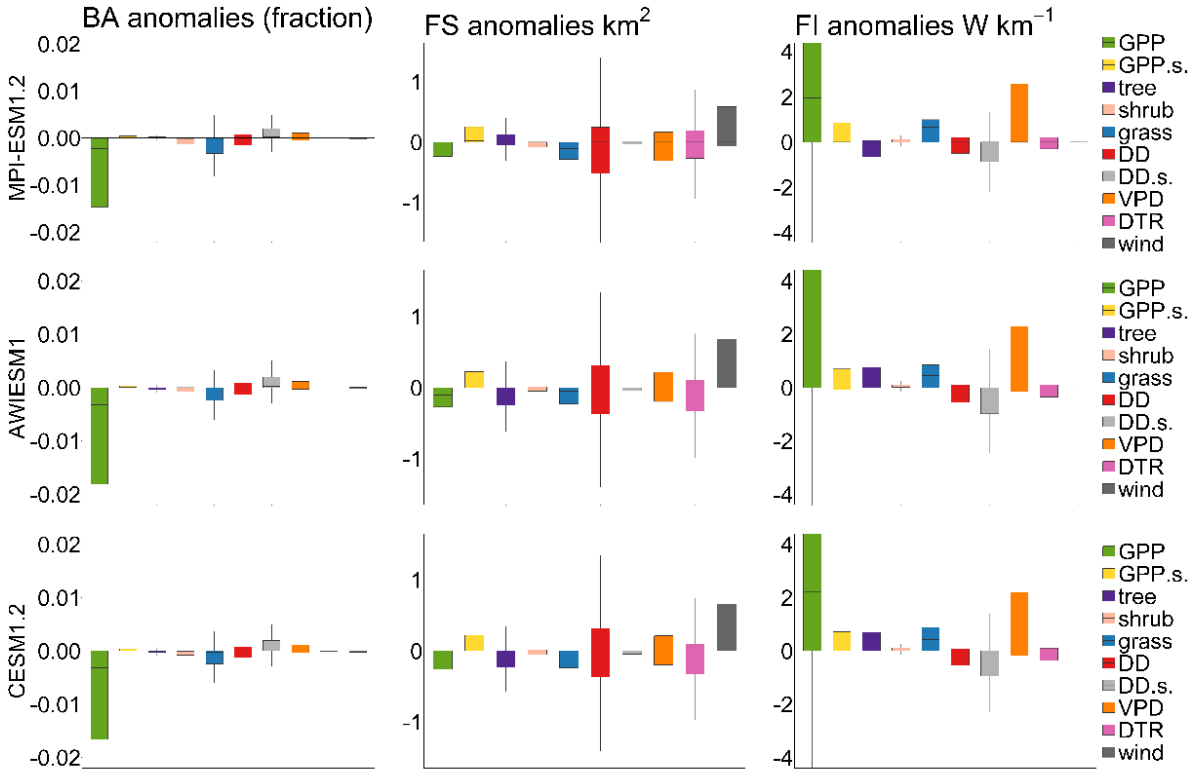

Figure S4.8. Boxplots showing relative importance of each predictor (GPP; gross primary production, GPP.s.; GPP seasonality, tree; tree cover, shrub; shrub cover, grass; grass cover, DD; dry days, DD.s.; dry days seasonality, VPD; vapour pressure deficit, DTR; diurnal temperature range, wind; wind speed) in driving the anomaly between the MOD 395 ppm and MOD 185 ppm experiment. For each grid cell common to both experiments (on modern-day continental shelves and masking the LGM ice sheets), the predictor which cause the largest change in the anomaly between the two experiments when it was excluded from the GLM model was retained, it is the change in anomaly that is shown here. This was taken as an indicator of relative importance of that predictor in driving the observed change for (a) the AWIESM1 LGM scenario, (b) the MPI-ESM-1.2 LGM scenario and (c) the CESM1.2 LGM scenario. A positive anomaly represents the variable driving an increase in BA, FS or FI at the LGM and a negative anomaly represents the variable driving a decrease in BA, FS or FI at the LGM.

S5. Comparison of experiments with the Reading Paleofire Database (RPD)

BA experiments		**MPI_ESM1.2**			**AWIESM1**			**CESM1.2 LGM**		
Scenario	RPD	LGM 190	MOD 190	LGM 395	LGM 190	MOD 190	LGM 395	LGM 190	MOD 190	LGM 395
Negative RPD anomalies										
Number of records	35	20	21	13	17	21	10	20	20	17
Successful identification (percentage)		57	60	37	49	60	29	57	57	49
Positive RPD anomalies										

Number of records	16	3	0	8	6	0	5	0	0	3
Successful identification (percentage)		19	0	50	38	0	31	0	0	19
Total RPD anomalies										
Number of records	51	23	21	21	23	21	15	20	20	20
Successful identification (percentage)		45	41	41	45	41	29	39	39	39

Table S5.1. Comparison of sign in BA anomalies (between the MOD climate/MOD CO_2 experiment and other three experiments respectively) at the location of each RDP (Harrison et al., 2022) charcoal-based reconstructions record. A positive anomaly represents increased biomass burning, and a negative anomaly represents decrease biomass burning. A successful identification means that the sign of the experiment anomaly and the sign of the RPD charcoal-based reconstructions are the same.

FS experiments		**MPI_ESM1.2**			**AWIESM1**			**CESM1.2 LGM**		
Scenario	RPD	LGM 190	MOD 190	LGM 395	LGM 190	MOD 190	LGM 395	LGM 190	MOD 190	LGM 395
Negative RPD anomalies										
Number records showing reduced burning	35	10	15	7	11	9	8	10	14	11
Successful identification (percentage)		29	43	20	31	26	23	29	40	31
Positive RPD anomalies										
Number records showing increased burning	16	6	2	7	8	8	9	4	2	4
Successful identification (percentage)		38	13	44	50	50	56	25	13	25
Total RPD anomalies										
Total number of records	51	16	17	14	19	17	17	14	16	15
Successful identification (percentage)		31	33	27	37	33	33	27	31	29

Table S5.2. Comparison of sign in FS anomalies (between the MOD climate/MOD CO_2 experiment and other three experiments respectively) at the location of each RDP (Harrison et al., 2022) charcoal-based reconstructions record. A positive anomaly represents increased biomass burning, and a negative anomaly represents decrease biomass burning. A successful identification means that the sign of the experiment anomaly and the sign of the RPD charcoal-based reconstructions are the same.

FI experiments		**MPI_ESM1.2**	**AWIESM1**	**CESM1.2 LGM**

Scenario	RPD	LGM 190	MOD 190	LGM 395	LGM 190	MOD 190	LGM 395	LGM 190	MOD 190	LGM 395
Negative RPD anomalies										
Number records showing reduced burning	35	5	7	9	7	7	11	3	5	4
Successful identification (percentage)		14	20	26	20	20	31	9	14	11
Positive RPD anomalies										
Number records showing increased burning	16	10	12	7	10	12	8	9	11	8
Successful identification (percentage)		63	75	44	63	75	50	56	69	50
Total RPD anomalies										
Total number of records	51	15	19	16	17	19	19	12	16	12
Successful identification (percentage)		30	37	31	33	37	37	24	31	24

Table S5.3. Comparison of sign in FI anomalies (between the MOD climate/MOD CO_2 experiment and other three experiments respectively) at the location of each RDP (Harrison et al., 2022) charcoal-based reconstructions record. A positive anomaly represents increased biomass burning, and a negative anomaly represents decrease biomass burning. A successful identification means that the sign of the experiment anomaly and the sign of the RPD charcoal-based reconstructions are the same.

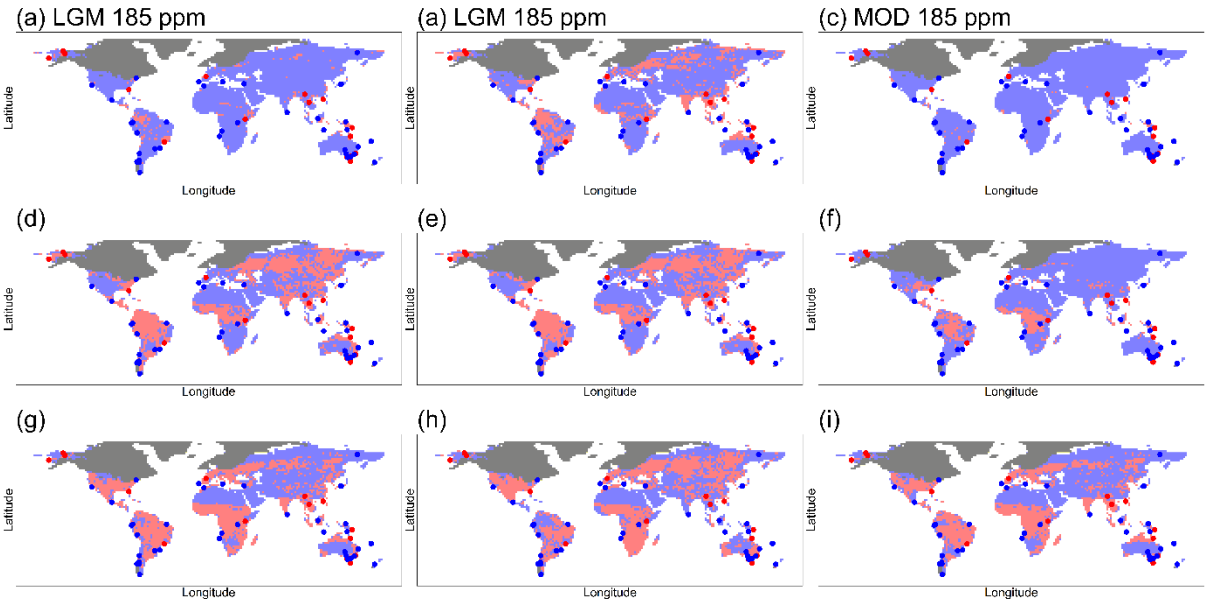

Figure S5.1 Comparison of anomalies between the experiment outputs from the MPI-ESM1.2 LGM scenario with the Reading Paleofire Database (RPD) for (a) the relatistic BA LGM experiment (b) the BA LGM

climate/MOD CO_2 sensitivity experiment and (c) the BA MOD climate/LGM CO_2 sensitivity experiment (d) the relatistic FS LGM experiment (e) the FS LGM climate/MOD CO_2 sensitivity experiment and (f) the FS MOD, (g) the relatistic FI LGM experiment (h) the FI LGM climate/MOD CO_2 sensitivity experiment and (i) the FI MOD climate/LGM CO_2 sensitivity experiment climate/LGM CO_2 sensitivity experiment. The modeled positive LGM-MOD anomalies are shown in red and LGM-MOD negative anomalies in blue. Dotted red (positive anomaly) and blue (negative anomaly) points show the location of the RPD records for the LGM. The LGM ice sheets are shown in dark blue.

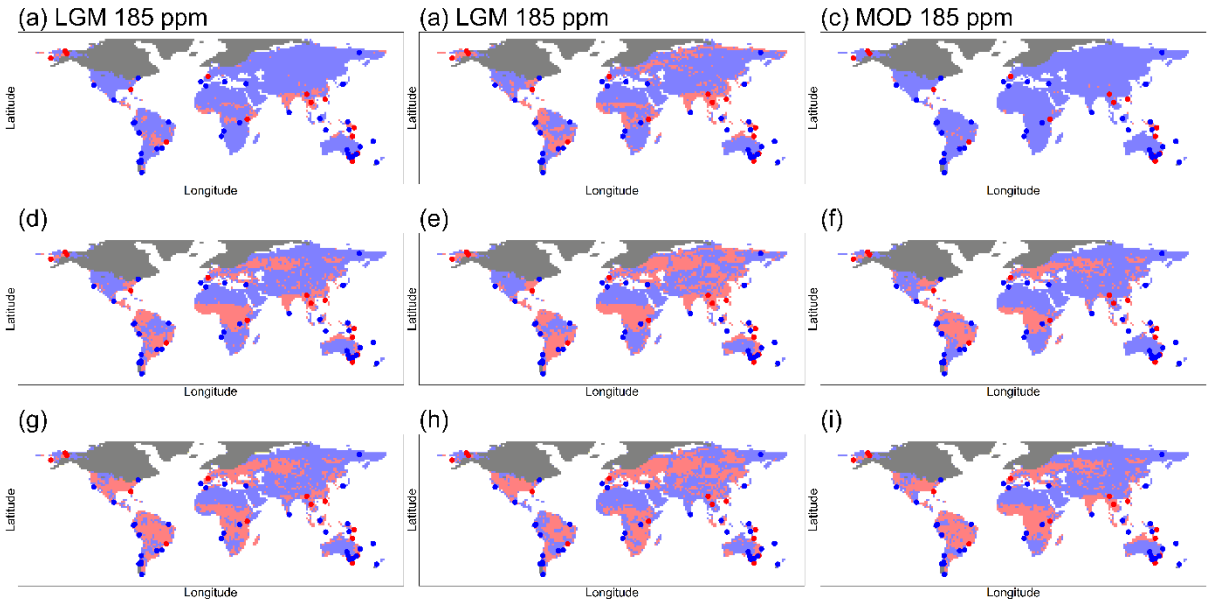

Figure S5.2 Comparison of anomalies between the experiment outputs from the AWIESM1 LGM scenario with the Reading Paleofire Database (RPD) for (a) the relatistic BA LGM experiment (b) the BA LGM climate/MOD CO_2 sensitivity experiment and (c) the BA MOD climate/LGM CO_2 sensitivity experiment (d) the relatistic FS LGM experiment (e) the FS LGM climate/MOD CO_2 sensitivity experiment and (f) the FS MOD, (g) the relatistic FI LGM experiment (h) the FI LGM climate/MOD CO_2 sensitivity experiment and (i) the FI MOD climate/LGM CO_2 sensitivity experiment climate/LGM CO_2 sensitivity experiment. The modeled positive LGM-MOD anomalies are shown in red and LGM-MOD negative anomalies in blue. Dotted red (positive anomaly) and blue (negative anomaly) points show the location of the RPD records for the LGM. The LGM ice sheets are shown in dark blue.

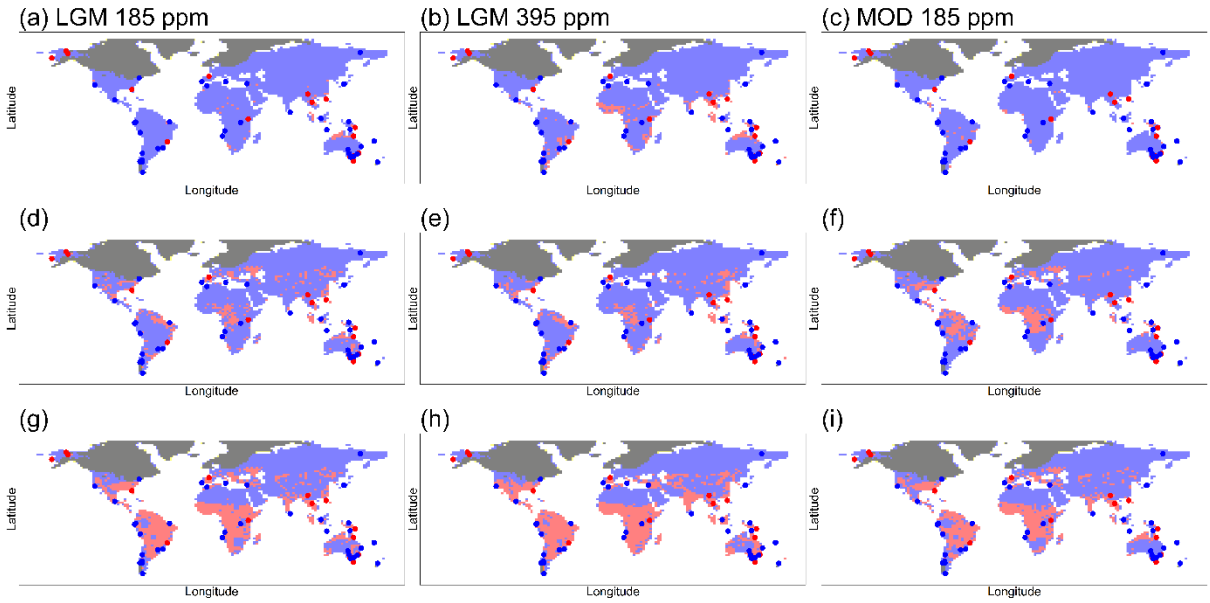

Figure S5.3 Comparison of anomalies between the experiment outputs from the CESM1.2 LGM scenario with the Reading Paleofire Database (RPD) for (a) the relatistic BA LGM experiment (b) the BA LGM climate/MOD CO_2 sensitivity experiment and (c) the BA MOD climate/LGM CO_2 sensitivity experiment (d) the relatistic FS LGM experiment (e) the FS LGM climate/MOD CO_2 sensitivity experiment and (f) the FS MOD, (g) the relatistic FI LGM experiment (h) the FI LGM climate/MOD CO_2 sensitivity experiment and (i) the FI MOD climate/LGM CO_2 sensitivity experiment climate/LGM CO_2 sensitivity experiment. The modeled positive LGM-MOD anomalies are shown in red and LGM-MOD negative anomalies in blue. Dotted red (positive anomaly) and blue (negative anomaly) points show the location of the RPD records for the LGM. The LGM ice sheets are shown in dark blue.

References

Bistinas, I., Harrison, S.P., Prentice, I.C. and Pereira, J.M.C,: Causal relationships versus emergent patterns in the global controls of fire frequency. *Biogeosciences*, *11*(18), pp.5087-5101, https://doi.org/10.5194/bg-11-5087-2014, 2014.

Bowman, D. M. J. S., Kolden, C. A., Abatzoglou, J. T., Johnston, F. H., van der Werf, G. R., and Flannigan, M.: Vegetation fires in the Anthropocene. *Nature Reviews Earth and Environment*, *1*(10), 500–515, https://doi.org/10.1038/s43017-020-0085-3, 2020.

Cucchi, M., Weedon, G. P., Amici, A., Bellouin, N., Lange, S., Müller Schmied, H., Hersbach, H., and Buontempo, C.: WFDE5: bias-adjusted ERA5 reanalysis data for impact studies. *Earth System Science Data*, *12*(3), 2097–2120, https://doi.org/10.5194/essd-12-2097-2020, 2020.

Gautney, J. R., and Holliday, T. W.: New estimations of habitable land area and human population size at the Last Glacial Maximum. *Journal of Archaeological Science*, *58*, 103–112, https://doi.org/10.1016/j.jas.2015.03.028, 2015.

Haas, O., Prentice, I. C., and Harrison, S. P.: Global environmental controls on wildfire burnt area, size, and intensity. *Environmental Research Letters*, *17*(6), 065004, https://doi.org/10.1088/1748-9326/ac6a69, 2022.

Harrison, S. P., Prentice, I. C., Bloomfield, K. J., Dong, N., Forkel, M., Forrest, M., Ningthoujam, R. K., Pellegrini, A., Shen, Y., and Baudena, M. Cardoso, A.W., Huss, J.C., Joshi J., Oliveras, I., Pausas, J.G. and Simpson, J.K.: Understanding and modelling wildfire regimes: an ecological perspective. *Environmental Research Letters*, *16*(12), 125008, https://doi.org/10.1088/1748-9326/ac39be, 2021.

Harrison, S. P., Villegas-Diaz, R., Cruz-Silva, E., Gallagher, D., Kesner, D., Lincoln, P., Shen, Y., Sweeney, L., Colombaroli, D., and Ali, A.: The Reading Palaeofire Database: an expanded global resource to document changes in fire regimes from sedimentary charcoal records. *Earth System Science Data*, *14*(3), 1109–1124, https://doi.org/10.5194/essd-14-1109-2022, 2022.

Kaplan, J. O., Bigelow, N. H., Prentice, I. C., Harrison, S. P., Bartlein, P. J., Christensen, T. R., Cramer, W., Matveyeva, N. V, McGuire, A. D., and Murray, D. F.: Climate change and Arctic ecosystems: 2. Modeling, paleodata-model comparisons, and future projections. *Journal of Geophysical Research: Atmospheres*, *108*(D19), https://doi.org/10.1029/2002JD002559, 2003.

Knorr, W., Jiang, L. and Arneth, A.,: Climate, CO_2 and human population impacts on global wildfire emissions. *Biogeosciences*, *13*(1), pp.267-282, https://doi.org/10.5194/bg-13-267-2016, 2016.

Knorr, W., Kaminski, T., Arneth, A. and Weber, U.,: Impact of human population density on fire frequency at the global scale. *Biogeosciences*, *11*(4), pp.1085-1102, https://doi.org/10.5194/bg-11-1085-2014, 2014.

Liu, L., Bestel, S., Shi, J., Song, Y., and Chen, X.: Paleolithic human exploitation of plant foods during the last glacial maximum in North China. *Proceedings of the National Academy of Sciences of the United States of America*, 110(14), 5380–5385. https://doi.org/10.1073/pnas.1217864110, 2013.

Marlon, J.R., Bartlein, P.J., Carcaillet, C., Gavin, D.G., Harrison, S.P., Higuera, P.E., Joos, F., Power, M.J. and Prentice, I.C.,: Climate and human influences on global biomass burning over the past two millennia. *Nature Geoscience*, 1(10), pp.697-702, https://doi.org/10.1038/ngeo313, 2008.

Pechony, O., and Shindell, D. T.: Driving forces of global wildfires over the past millennium and the forthcoming century. *Proceedings of the National Academy of Sciences*, 107(45), 19167-19170, https://doi.org/10.1073/pnas.1003669107, 2010.

Saitoh, T. M., Nagai, S., Noda, H. M., Muraoka, H., and Nasahara, K. N., Examination of the extinction coefficient in the Beer–Lambert law for an accurate estimation of the forest canopy leaf area index. *Forest Science and Technology*, *8*(2), 67–76, https://doi.org/10.1080/21580103.2012.673744, 2012.

Tallavaara, M., Luoto, M., Korhonen, N., Järvinen, H. and Seppä, H.,: Human population dynamics in Europe over the Last Glacial Maximum. *Proceedings of the National Academy of Sciences*, *112*(27), pp.8232-8237, https://doi.org/10.1073/pnas.1503784112 ,2015.